Surface-induced morphology and free-energy pathways in breakup of a nematic liquid crystalline cylinder

Rajesh K. Goyal and Morton M. Denn
Benjamin Levich Institute for Physico-Chemical Hydrodynamics and Department of Chemical Engineering, City College of New York, CUNY, New York, New York 10031, USA

(Received 28 January 2008; published 11 August 2008)

We compute the surface-induced morphology and the free-energy pathways as a cylindrical liquid crystalline filament with preferred homeotropic (orthogonal) interface orientation passes through a sequence of growing sinusoidal perturbations and breaks up into droplets. Liquid crystalline morphology is determined using a simulated annealing algorithm [R. K. Goyal and M. M. Denn, Phys. Rev. E, **75**, 021704 (2007)] to minimize the Oseen-Frank free energy. A first-order morphological transition with a finite energy barrier is required when the perturbation amplitude exceeds a critical value, and it is possible that progress towards breakup will be kinetically trapped in a varicose cylindrical shape. This result may be related to the apparent kinetic trapping of dispersed nematic 4′-octyl-4-biphenylcarbonitrile in a gel state reported by Inn and Denn [J. Rheol., **49**, 887 (2005)].

DOI: 10.1103/PhysRevE.78.021706 PACS number(s): 61.30.Gd, 61.30.Pq

I. INTRODUCTION

A. Nematic droplets

Dispersions of nematic liquid crystalline droplets in a polymeric matrix are of interest in many areas of science and engineering, including device technology. The functional properties of these multiphase systems often depend on the liquid crystalline orientation distribution in the droplet, which is determined by a balance between the bulk nematic potential, which favors alignment, and the surface potential, which often favors an orthogonal (homeotropic) orientation. The orientational issues in liquid crystalline droplets are discussed in the book by Drzaic [1] and in a brief review by Lavrentovich [2].

Multiple locally stable states can exist in liquid crystalline dispersions. We have observed bistability in a dispersion of 4′-octyl-4-biphenylcarbonitrile (8CB) in polydimethylsiloxane [3], for example, where a bicontinuous gel-like morphology and dispersed droplets with a radial conformation can both exist within the nematic temperature regime. The dispersed droplet morphology appears to be the lower free-energy state for the nematic, but the gel breaks up into a low-viscosity dispersed droplet system only when the temperature is raised above the nematic-isotropic transition. We have speculated that an extended liquid crystalline structure that creates the gel is kinetically trapped because of a large energy barrier between the extended and spherical states, both with homeotropic orientation. In a previous paper [4] we explored the orientational morphologies of spherical and spheroidal droplets of nematic liquid crystals using a simulated annealing approach, with particular attention to bistability, the transitions between locally stable states, and the energy barriers for such transitions. Here, we extend this approach to liquid crystalline cylinders and to the development of pathways by which a liquid crystalline cylinder might break up into droplets.

The breakup of cylinders of isotropic liquids into droplets is driven by interfacial tension. Rayleigh first showed that an infinitely long circular cylinder comprising an incompressible Newtonian liquid will break up into spherical droplets if the wavelength of infinitesimal sinusoidal perturbations is larger than some minimum value, equal to the circumference of the cylinder for an inviscid liquid; the problem is addressed in detail by Chandrasekhar [5]. Tomotika [6] analyzed capillary instabilities in an isotropic viscous matrix, including the effect of the fiber-to-matrix viscosity ratio. Rey [7] recently studied the stability of incompressible nematic fibers, taking into account the nematic orientation and the matrix-to-fiber viscosity ratio. Our approach differs from the classical treatment of stability, in that we assume that any breakup will occur because of finite sinusoidal disturbances of the nematic cylinder, and we calculate the equilibrium free energies of the perturbed states. In this way we can define feasible pathways by which a transition from cylinder to droplets can occur through a monotonic decrease in free energy, and we can determine any energy barriers that must be overcome along such a path.

B. Free energy

Nematic liquid crystal orientation is described in the continuum theory developed by Oseen and Frank [8] in terms of a position-dependent unit vector **n**, known as the "director." The free-energy density of a bulk nematic is given by

$$f = \frac{1}{2}\{k_{11}(\nabla \cdot \mathbf{n})^2 + k_{22}(\mathbf{n} \cdot \nabla \times \mathbf{n})^2 + k_{33}(\mathbf{n} \times \nabla \times \mathbf{n})^2 - k_{24}\nabla \cdot [\mathbf{n} \times \nabla \times \mathbf{n} + \mathbf{n}(\nabla \cdot \mathbf{n})]\}, \quad (1)$$

where the parameters k_{11}, k_{22}, k_{33}, and k_{24} are the Frank elastic constants associated with splay, twist, bend, and saddle-splay distortions, respectively. (Our k_{24} is twice the saddle-splay coefficient defined by Kleman and Lavrentovich [8].) A mixed splay-bend term with an elastic coefficient k_{13} is usually neglected because it involves higher-order derivatives of the director field; the saddle-splay term in Eq. (1) appears to be higher order but in fact reduce to first deriva-

tives of the vector field. The saddle-splay term is a divergence that can be transformed into a surface integral; the term is often neglected in calculations, but it may be important in nonplanar geometries. **n** and **−n** must be equivalent in a nematic.

When all four elastic constants are equal, or when three constants are equal and k_{24} is taken to be zero, the bulk free-energy density simplifies to

$$f = \frac{1}{2}K(\nabla \cdot \mathbf{n}):(\nabla \cdot \mathbf{n})^T, \tag{2}$$

where K is the single elastic coefficient. The assumption of equal constants is only approximate for real liquid crystals; for 5CB (4′-pentyl-4-biphenylcarbonitrile), for example, values of k_{33}/k_{11} between 1.3 and 1.6 and values of k_{22}/k_{11} between 0.48 and 0.66 have been reported [8–10]. The ratio k_{33}/k_{11} appears to be of order 0.1 and k_{22}/k_{11} less than 10^{-2} in liquid crystalline polymers [11]. Saddle-splay effects are reviewed broadly in Crawford and Žumer [12]. Data for k_{24} are quite limited, and the Cauchy relation $k_{24}=\frac{1}{2}(k_{11}+k_{22})$ [13] is often assumed.

The surface free energy density of a nematic with a preferred homeotropic orientation at the interface is usually given by the one-constant Rapini-Papoular [14] form

$$f_S = \frac{1}{2}W \sin^2 \varphi. \tag{3}$$

Here, φ is the angle that the director makes with the preferred orientation and W determines the strength of the anchoring. This is a convenient functional form for the surface free energy, in that it is bounded and approximates a leading order quadratic term for small angles.

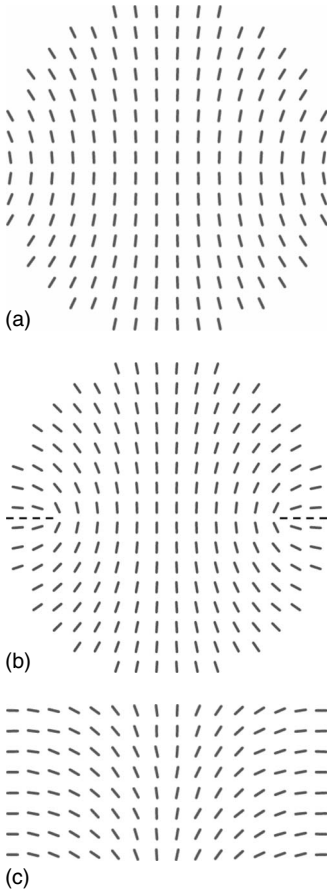

FIG. 1. Schematics of orientations observed in nematic cylinders: (a) planar-polar (cross section orthogonal to cylinder axis), (b) planar-polar with line defect (cross section orthogonal to cylinder axis), and (c) escaped-radial (cross section parallel to cylinder axis).

C. Transitions

The equilibrium nematic orientation in a dispersed phase is determined by the relative strengths of the surface and bulk forces. We recently calculated transitions between radial and parallel orientations in spherical and spheroidal liquid crystals with homeotropic surface orientation [4]. The total free energy in a spherical droplet with a perfect radial orientation is $4\pi R(2k_{11}-k_{24})$, while the total free energy with a perfect parallel orientation is $4\pi WR^2/3$. Hence, the radial orientation is energetically favored if $WR/(2k_{11}-k_{24})>3$ and the parallel orientation is favored if $WR/(2k_{11}-k_{24})<3$, with an orientational transition that is expected to be first order when $WR/(2k_{11}-k_{24})$ is equal to 3. We find computationally that the transition occurs when $WR/(2k_{11}-k_{24})$ is between 4.5 and 7.3, depending on the values of the elastic coefficients; the deviation from the ideal value of 3 occurs because the "perfect" orientations are not possible.

The expected orientations in a cylindrical liquid crystal with homeotropic orientation in which all elastic coefficients have comparable magnitudes are planar-polar (PP), planar-polar with line defects (PPLD), and escaped radial (ER), as shown schematically in Fig. 1. The orientations in the PP and PPLD configurations are entirely in the plane, where the latter exhibits symmetric line singularities to accommodate radial orientation at the equator. The ER orientation is radial in the plane near the cylindrical surface, but with an out-of-plane transition near the centerline in place of a line singularity. Analytical solutions for the total nematic free energy for PP and ER orientations in a cylindrical liquid crystal with $k_{11}=k_{33}$ and homeotropic surface orientation are as follows [15]:

$$\text{PP: } E = \pi k_{11} L\left(2 - \left[1 + \frac{1}{4}\left(\frac{WR}{k_{11}}\right)^2\right]^{1/2} - \ln\left\{\frac{4k_{11}}{WR}\left[4\left(\frac{k_{11}}{WR}\right)^2 + 1\right]^{1/2} - 8\left(\frac{k_{11}}{WR}\right)^2\right\}\right), \tag{4a}$$

$$\text{ER: } E = \begin{cases} \pi k_{11} L \left[3 - \frac{k_{24}}{k_{11}} - \left(\frac{WR}{k_{11}} + \frac{k_{24}}{k_{11}} - 1 \right)^{-1} \right], & \frac{WR}{k_{11}} > 2 - \frac{k_{24}}{k_{11}}, \\ \pi RWL, & \frac{WR}{k_{11}} < 2 - \frac{k_{24}}{k_{11}}. \end{cases} \tag{4b}$$

The transition between these states depends on the value of k_{24}; for $k_{24}=k_{11}$, for example, the ER orientation is energetically favored if $WR/k_{11}>8.65$ and the PP orientation if $WR/k_{11}<8.65$.

II. COMPUTATIONAL ALGORITHM

A. Free energy minimization

The equilibrium director field $\mathbf{n}(\mathbf{r})$ in a given geometry minimizes the total free energy, which is the sum of the volume integral of f [Eq. (1)] and the surface integral of f_S [Eq. (3)], with the constraints that $\mathbf{n}$ is a unit vector and the states $\mathbf{n}$ and $-\mathbf{n}$ are indistinguishable. The simulation algorithm and discretization issues have been discussed in our previous paper [4]. Briefly, the droplet is circumscribed by a rectangular parallelepiped that is discretized into cubes of equal volume, and the vector field $\mathbf{n}$ is defined by a discrete value in each element. Straightforward discretization of the free energy density in Eqs. (1) or (2) results in loss of equivalence of $\mathbf{n}$ and $-\mathbf{n}$, and we follow a procedure by Gruhn and Hess [16] to retain nematic symmetry. We implement both forward and backward differences to approximate derivatives and average over two nearest-neighbor terms.

We use simulated annealing to find the minimizing vector field $\mathbf{n}$ in a liquid-crystal droplet. The system is initialized by choosing the vectors $\mathbf{n}(i,j,k)$ either randomly or with a specific distribution (a parallel or radial orientation, for example). We then randomly select a lattice cell and randomly change the orientation of the director within that cell; this move affects the free energy density in the selected cell and the six nearest neighbors. The new director orientation is accepted or rejected according to Metropolis sampling, in which the new orientation is accepted with probability $p(\mathbf{n}_{\text{old}} \rightarrow \mathbf{n}_{\text{new}}) = \min[1, \exp(-\Delta E / k_B T)]$. The Monte Carlo temperature T in our simulations is dependent on the lattice spacing and is not a real physical variable. We initially fix the Monte Carlo temperature at a high value to keep the system from becoming trapped in a local minimum, and the temperature is then gradually decreased.

To increase the efficiency of the algorithm, we introduce a scale factor to restrict the magnitude of the change in the orientation of $\mathbf{n}$ as the system approaches the global free-energy minimum. The scale factor permits acceptance of about 50% of the trial moves during the simulations. The evolution of the total free energy and other observables are obtained by computing averages over a specified number of MC cycles, typically 20 000. The calculations are carried out in dimensionless form.

B. Order parameters

Nematic order is conventionally described by a global order parameter $S_{\parallel}$, which equals unity when all directors are parallel and zero when the directors are oriented randomly or radially, and an orthogonal order parameter $S_{\perp}$, which equals unity for a radial orientation and zero for a parallel orientation. The calculations of $S_{\parallel}$ and $S_{\perp}$ have been discussed in Ref. [4].

In a cylindrical geometry we also calculate an escaped-radial order parameter, as defined by Smondyrev and Pelcovits [17], which we denote S_{ER}:

$$S_{\text{ER}} = \frac{1}{N} \left\langle \sum_{i=1}^{N} \left[\frac{3}{2} (\mathbf{n}_i \cdot \mathbf{z}_i)^2 - \frac{1}{2} \right] \right\rangle. \tag{5}$$

The cylinder axis is along the z direction. S_{ER} measures the degree of escape from the plane perpendicular to the cylinder axis; thus, S_{ER} equals $-1/2$ for a PP orientation and unity for a uniform orientation parallel to the cylinder axis. In the case of an ER orientation, $S_{\perp}$ and S_{ER} can take both negative and positive values.

III. SPHERICAL DROPLETS

Our overall approach in seeking to understand transitions from cylindrical liquid crystalline structures to spherical droplets is to follow the morphology and free energy through a series of shapes, from cylinder to increasingly perturbed cylinder to spherical droplet, seeking paths through which the equilibrium free-energy continuously decreases. We have previously studied spherical droplets with a preferred orthogonal surface orientation [4]. For equal elastic coefficients, a first-order transition from a nearly parallel conformation to a radial conformation is observed at a critical value of WR/K of just under 6. Simulated optical micrographs of the equilibrium director orientation distributions for values of WR/K below and above the transition are shown in Figs. 2(a) and 2(b), respectively. (A standard Jones matrix method was used to calculate simulated optical micrographs, as discussed in Refs. [1,18,19].)

The radial morphology is clearly revealed through the Maltese cross image in Fig. 2(b). Both states are locally stable to small fluctuations over the entire range of WR/K, however. The difference between the free energy of the equilibrium state and the maximum free energy along a feasible path that is defined by continuously changing the Monte Carlo temperature starting from the local minimum provides an upper bound for the energy barrier between the local and global minima; the maximum corresponds to an energy density of about 2000 J/m^3 for a droplet with a radius of 1 μm and a typical elastic coefficient of 5×10^{-12} N.

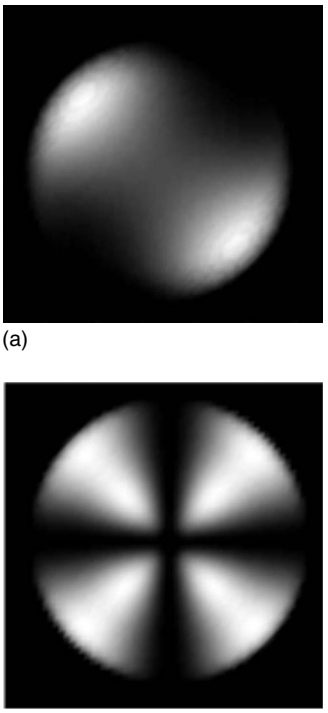

FIG. 2. Simulated polarized optical micrographs for spherical droplets with homeotropic anchoring. (a) $WR/K=4.2$ and (b) $WR/K=6.0$.

IV. CYLINDRICAL DROPLETS

A. Equal elastic coefficients

We first discuss results for a circular cylinder with equal elastic coefficients. Periodic boundary conditions were established at the open ends of the cylinder, and we used random initial conditions for the director and an initial MC temperature close to the computed isotropic-nematic transition to permit large fluctuations. The calculated total free energy normalized by $2\pi KL$ [Eq. (4b) for $WR/K\rightarrow\infty$] is shown in Fig. 3 as a function of WR/K for cylindrical cavities with different length/radius (L/R) ratios. (The number of lattice

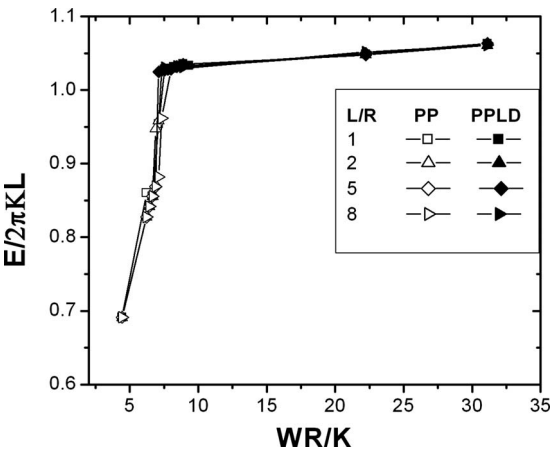

FIG. 3. Total free energy for homeotropic nematic cylinders when simulations are started with a random initial state.

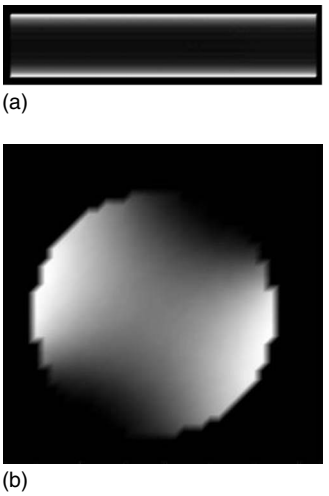

FIG. 4. Simulated optical micrographs in nematic cylinders for $WR/K=4.44$, planar-polar orientation. (a) Image when light propagates perpendicular to the cylinder axis and (b) image when light propagates along the cylinder axis.

cells scales linearly with L/R; $L/R=5$ requires 124 696 cells.) There is clear convergence with respect to length of the cylinder, and there is a sharp change in free energy at a value of WR/K of about 7. A planar-polar structure is obtained for low WR/K, as expected, while strong anchoring exhibits a planar-polar structure with two line defects (PPLD) near the interface. Simulated optical micrographs of the equilibrium orientation distributions below and above the transition are shown for $WR/K=4.44$ and 1000 in Figs. 4 and 5, respectively.

The computed normalized free energy for the PPLD structure for large WR/K is higher than the asymptotic value of unity given by Eq. (4b) for the escaped radial structure. We were unable to obtain an ER structure with our simulated annealing algorithm starting from random initial conditions. A similar observation was made by Smondrev and Pelcovits

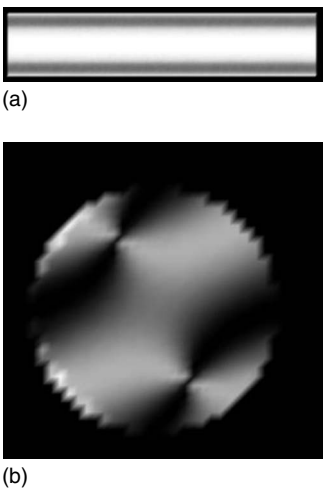

FIG. 5. Simulated optical micrographs in nematic cylinders for $WR/K=1000$, planar-polar orientation with two defects. (a) Image when light propagates perpendicular to the cylinder axis and (b) image when light propagates along the cylinder axis.

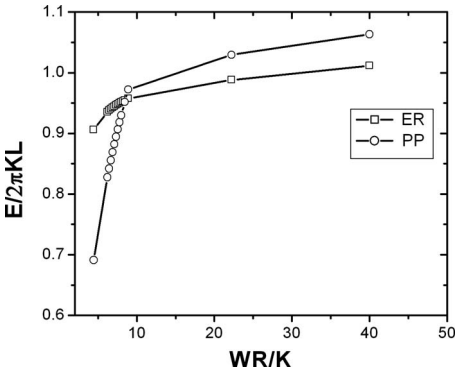

FIG. 6. Total free energy of nematic cylinders for planar-polar and escaped-radial orientations.

[17] and Chicoli *et al.* [20] in Monte Carlo simulations of the analogous molecular theory. It appears that the system always becomes trapped in a local minimum.

The free energies computed using the analytical expressions for PP and ER orientations as initial conditions, with low Monte Carlo temperatures to keep fluctuations small, are shown in Fig. 6. The PP structure is still found to be energetically favorable for small values of WR/K, while the ER structure is favored for large values of WR/K. A simulated optical micrograph of the ER configuration for $WR/K=20$ is shown in Fig. 7, where the escape line along the cylindrical axis is evident. The intensity of escape is high close to the cylinder axis but decreases towards the boundary. The calculated order parameters S_{ER} and $S_{\|}$ corresponding to the minimum free energy states are shown in Fig. 8. The critical value of WR/K at the transition between ER and PP morphologies lies between 8.44 and 8.89, which is close to the analytical value of 8.65 obtained above. (As shown in Fig. 3, the algorithm predicts a PP-PPLD transition at about $WR/K=7$, so we might expect to find PPLD structures for WR/K between 7 and 8.65.)

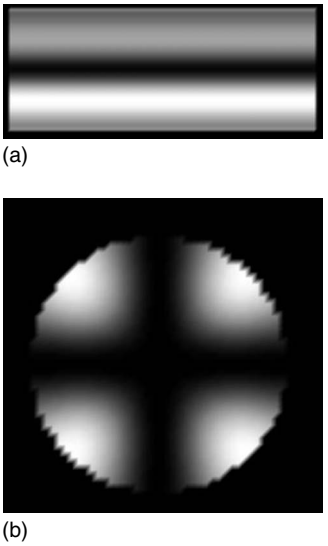

FIG. 7. Simulated optical micrographs for escaped-radial orientation in nematic cylinders for $WR/K=20$. (a) Image when light propagates perpendicular to the cylindrical axis and (b) image when light propagates along the cylindrical axis.

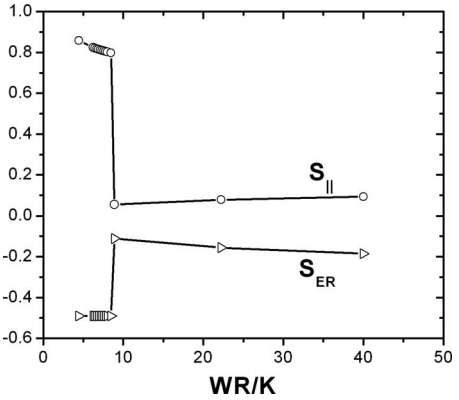

FIG. 8. Order parameters corresponding to minimum free-energy state for nematic cylinders with homeotropic orientation.

B. Multiplicity

We have found orientational multiplicities in cylinders similar to those observed in spheroids [4] by starting simulated annealing calculations with an ER distribution when WR/K is less than the transition value and with a PP distribution when WR/K is greater than the transition value, always keeping the Monte Carlo temperature small. In such cases we obtain convergence to a local minimum in the free energy; in the former case the local minimum free energy state is escaped radial, while in the latter it is a PP state with increasing distortion as WR/K is increased. As with the spheroids, we have estimated the free-energy barrier between the local and global minima by initializing the system in the local minimum and then gradually increasing the Monte Carlo temperature until the transition occurs. The sequence of states in the S_{ER}-$S_{\perp}$ plane in passing from a locally stable ER configuration to the globally minimal PP state, together with the corresponding free energies as a three-dimensional curve, are shown in Fig. 9 for $WR/K=4.44$, and simulated micrographs of the transition states are shown in Fig. 10. The transition from the escaped-radial structure initiates at one end of the cylindrical computational domain and propagates axially. The sequence is different during a transition from escaped radial to planar polar with weak anchoring (not shown here); in this case the escaped-radial structure first transforms into a parallel orientation along the cylinder axis. We could not carry out the corresponding calculation from PP to ER because the system always went to a PPLD orientation, as noted above.

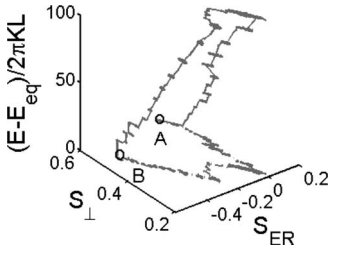

FIG. 9. Path in conformation space and corresponding free energy in passing from a locally stable escaped-radial orientation (A) to the planar-polar free energy minimum state (B).

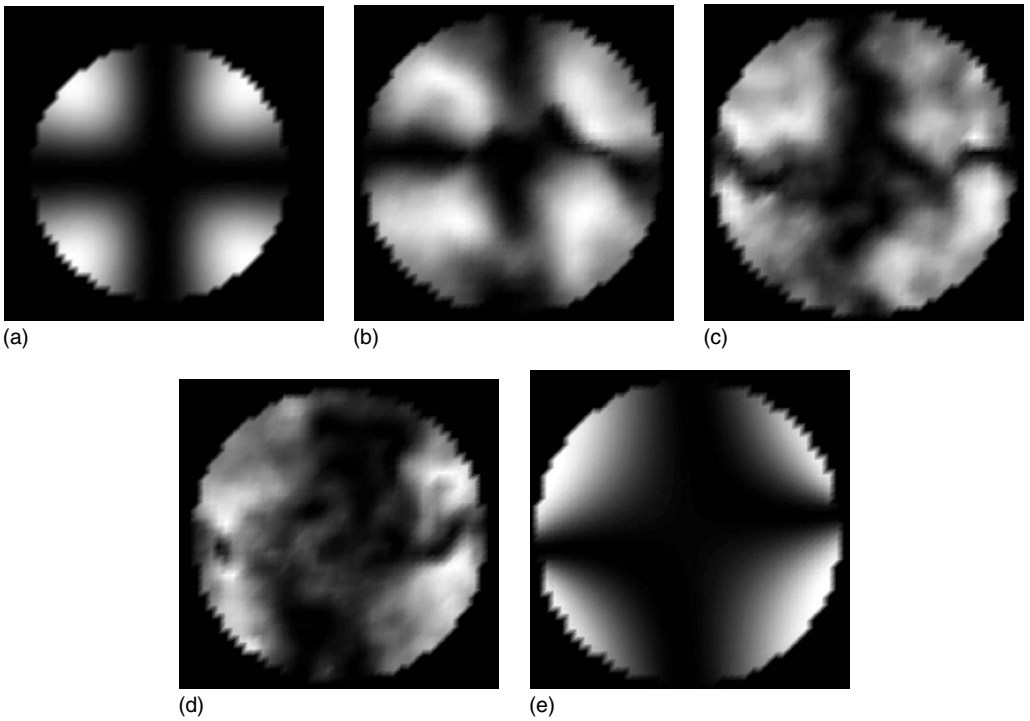

FIG. 10. (a)–(e) Defect development during the transition from a locally stable escaped-radial conformation to the equilibrium planar-polar conformation $WR/K=4.44$.

The estimated free energy barrier is shown as a function of WR/K in Fig. 11 for transitions from a locally stable ER configuration to the minimizing PP configuration. The maximum corresponds to an energy density of about 550 J/m^3 (Pa) for a typical elastic coefficient of 5×10^{-12} N and a cylinder with a radius of 1 μm. This free-energy density is less than that for the transition between radial and aligned configurations in spheres, but it is comparable to the computed barrier for elongated spheroids [4].

C. Unequal elastic constants

We have examined the effect of unequal coefficients on the director orientation in nematic cylinders using elastic constants typical of 5CB at room temperature: $k_{33}/k_{11}=1.31$, $k_{22}/k_{11}=0.51$, and $k_{24}=(k_{11}+k_{22})/2$. We initiated the simulations with both planar-parallel and escaped-radial orientations, comparing the free energies of the converged states to determine the minimum. The overall features of the computations are similar to those for equal elastic constants and are not documented here. Bend distortions in the PP orientation are small relative to the equal constant case because of the relatively large value of the bend elastic coefficient. The radial order parameter $S_\perp$ for $WR/(2k_{11}-k_{24})=8$, where the PP orientation is the minimizing state, is only 0.21, for example, compared to a value of 0.60 for equal constants.

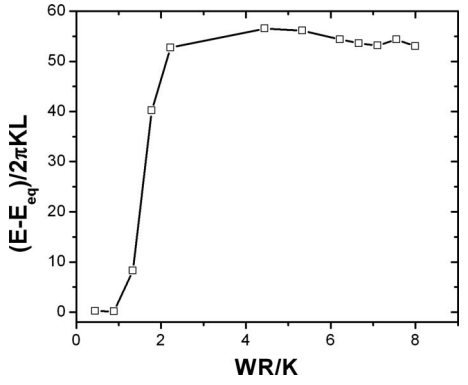

FIG. 11. Estimated energy barrier for the ER-PP transition as a function of WR/K.

V. PERTURBED CYLINDERS

A. Minimum free-energy morphologies

We now consider perturbed cylinders with radii of the form $R(z)=R_0+b\sin(2\pi z/\lambda)$, where z is measured along the cylinder axis. R_0 is the radius of the unperturbed cylinder, b is the perturbation amplitude, and λ is the wavelength of the perturbation. The ratio b/R_0 defines the magnitude of the relative perturbation; when $b/R_0=1$ we presume that the cylinder has broken up into droplets.

We carried out simulated annealing calculations for different values of λ and b using a variety of starting orientations: parallel to the cylinder axis, parallel in the orthogonal plane, deformed escaped radial (obtained by an affine transformation of a cylinder with an escaped-radial orientation), and deformed spherical radial, with a singularity on the cylinder axis at the center of the cycle. The calculated escaped-radial order parameters S_{ER} corresponding to the minimum free energy states are shown as functions of WR_0/K in Figs. 12(a)–12(c) for $\lambda/R_0=1$, 2, and 5, respectively, and various

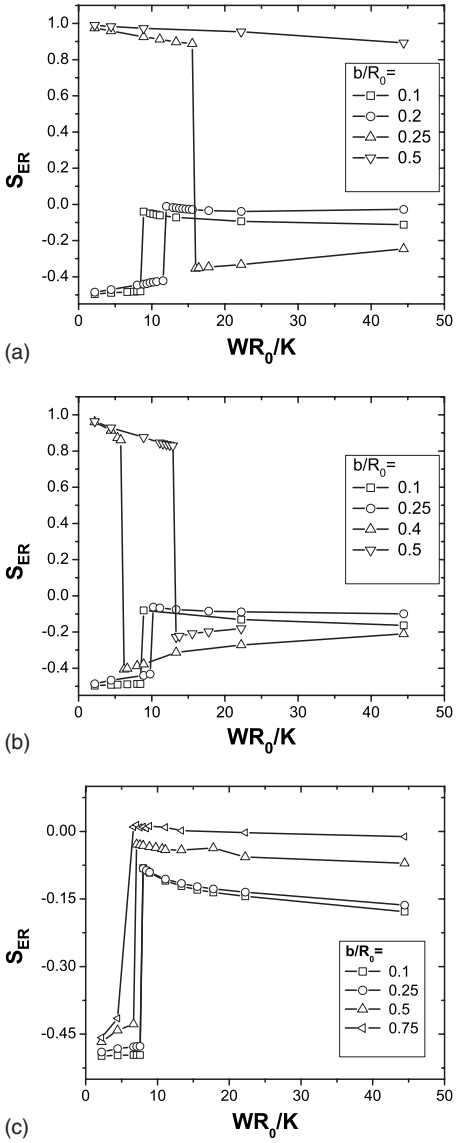

FIG. 12. Escaped-radial order parameter as a function of WR_0/K for perturbed cylinders. (a) $\lambda/R_0=1$, (b) $\lambda/R_0=2$, and (c) $\lambda/R_0=5$.

values of b/R_0. For small perturbation amplitudes or long wavelengths the perturbed and unperturbed cylinders have the same morphologies: weak anchoring favors a PP orientation while strong anchoring favors an ER orientation. With increasing perturbation amplitude there is a transition at long wavelengths to a deformed radial orientation, while at shorter wavelengths the dominant orientation is parallel to the cylinder axis except near the interface. Typical simulated optical micrographs are shown in Figs. 13 for very strong anchoring ($WR_0/K=1000$); the similarity between the deformed radial structure in Fig. 13(c) for $\lambda/R_0=5$ and $b=0.75$ and the radial orientation in a sphere shown in Fig. 2(b) is evident.

We plot the normalized minimum nematic free energies of deformed cylinders as functions of the perturbation magnitude in Fig. 14 for $WR_0/K=1000$. (We neglect the changing contribution to the total free energy from the isotropic interfacial tension as the geometry changes. As discussed below, this contribution is unimportant in the nematic regime.) The

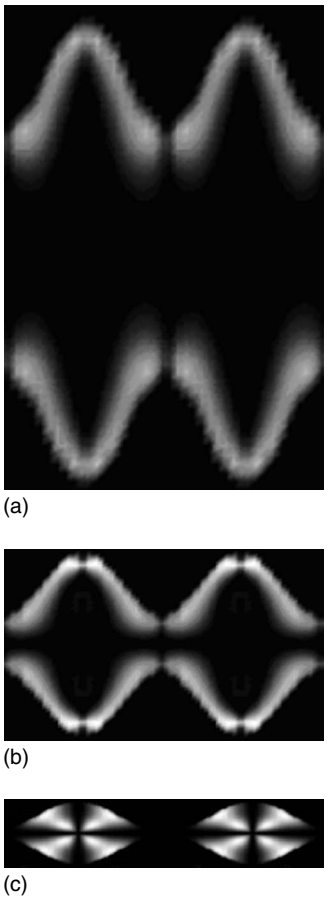

FIG. 13. Simulated optical micrographs for perturbed cylinders with strong homeotropic anchoring. (a) $\lambda/R_0=1$, $b/R_0=0.3$; (b) $\lambda/R_0=2$, $b/R_0=0.5$; (c) $\lambda/R_0=5$, $b/R_0=0.75$.

free energy increases with increasing perturbation amplitude for small wavelength disturbances ($\lambda/R_0 \leqslant 3$), hence such disturbances should not grow. The free energy decreases with increasing perturbation amplitude for cylinders with long wavelength disturbances ($\lambda/R_0 \geqslant 4$), however, indicating that perturbation growth is energetically favored and that the nematic cylinders should break up into droplets. The normalized free energies are plotted as functions of WR_0/K in Figs.

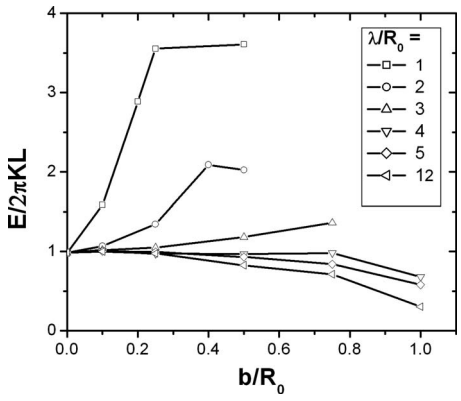

FIG. 14. Free energy as a function of deformation amplitude for nematic liquid crystalline filaments with perturbation wavelength λ $WR_0/K=1000$.

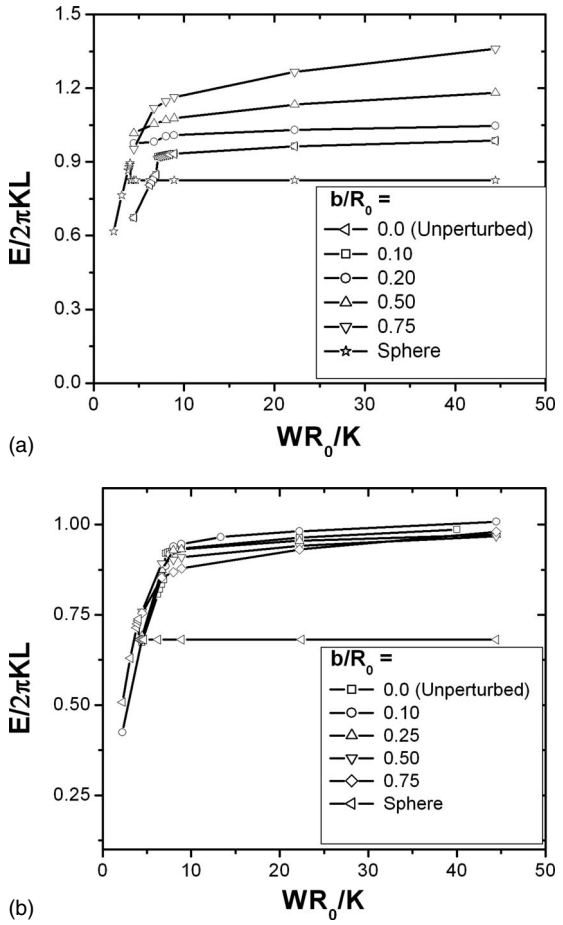

FIG. 15. Free energy as a function of WR_0/K for nematic liquid crystalline filaments with perturbation amplitude b and wavelength (a) $\lambda/R_0=3$ and (b) $\lambda/R_0=4$.

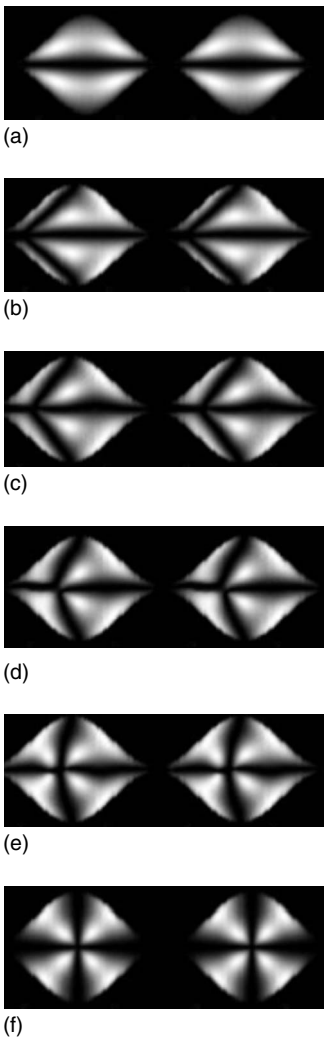

FIG. 16. (a)–(f) Morphological transition in passing from a locally stable escaped-radial orientation to radial equilibrium orientation; $\lambda/R_0=5$, $b/R_0=0.75$.

15(a) and 15(b) for $\lambda/R_0=3$ and 4, respectively, together with the free energy of a sphere having the volume contained in one wavelength. For strong anchoring, where the minimum free-energy state for the cylinder is escaped radial, breakup into spheres is always favored energetically, but a feasible path with monotonically decreasing free energy is possible only for the larger wavelength. A cylinder with weak anchoring is energetically more favorable than the equivalent spheres.

B. Morphological transition and energy barrier

The progression from a circular cylinder to breakup through a sequence of feasible minimum free energy states requires a morphological transition from escaped radial to radial; the latter is the morphology that exists in a sphere for strong anchoring and, as shown in Fig. 13(c), is also the morphology for a sinusoidally perturbed cylinder with a large wavelength and a large perturbation amplitude. Figure 16 shows simulated optical micrographs of the transition pathway for $\lambda/R_0=5$ and $b/R_0=0.75$ as the Monte Carlo temperature is first increased and then decreased to permit the transition from a locally stable deformed escaped-radial structure to the minimum free energy deformed radial structure. A singularity is generated at one end of the cycle, which then propagates to the center. The maximum energy barrier in this case corresponds to about 2400 J/m^3 for an equivalent droplet with a radius of 1 μm, which is comparable to the maximum transition energy for a sphere.

C. Isotropic interfacial tension

We have not accounted for the contribution of the isotropic interfacial tension to the total free energy in these calculations. The isotropic interfacial tension between nematic 8CB and PDMS as measured by pendant drop microscopy is about 2.3 mN/m [21], which is an order of magnitude larger than the maximum reported value for the anchoring parameter W [1], so it is not obvious that the isotropic term can be neglected. The major effect of the anchoring term in the strong anchoring regime is the determination of the bulk morphology, however, so direct comparison of magnitudes of the two surface terms is not relevant. Breakup of isotopic liquid cylinders occurs because the isotropic interfacial free energy grows with small wavelength disturbances and decreases with large wavelength disturbances, mirroring the

overall behavior of the nematic term. The total change in the isotropic term in passing from one wavelength of a perturbed cylinder to a sphere of equal volume is negligible for a nematic relative to the conformational free energy barrier that must be crossed, however; for a 1 μm perturbed cylinder with $\lambda/R_0=5$, for example, the isotropic interfacial free energy change is 230 J/m^3, compared to a free energy barrier of 2400 J/m^3 to effect the conformational transition.

VI. CONCLUSION

There are feasible paths with decreasing equilibrium free energies by which a nematic filament with strong homeotropic surface orientation can progress through a sequence of growing sinusoidal perturbations until it breaks up into nematic droplets. A morphological transition is required, however, in order to pass from the escaped radial orientation favored for cylinders to the radial orientation favored for strongly varicose distorted cylinders and spheres. The activation energy density for this transition is finite, and it is possible that progress towards breakup will be kinetically trapped in a varicose cylindrical shape without the possibility of breakup; in that case, breakup can only occur by raising the temperature sufficiently high to permit large orientational fluctuations, perhaps past the nematic-isotropic transition. Such varicose distortions on filaments were observed by Rueda and Shaw [22] in a blend of a nematic polymer in an isotropic matrix, although direct comparison is not appropriate because the Oseen-Frank theory used here is not appropriate for liquid crystalline polymers. This energy barrier may be related to the kinetic trapping of a dispersion of nematic 8CB in a gel state observed by Inn and Denn [3].

ACKNOWLEDGMENTS

This research was supported in part by the National Science Foundation under Grant No. CTS-0112358.

[1] P. S. Drzaic, *Liquid Crystal Dispersions* (World Scientific, Singapore 1995).
[2] O. D. Lavrentovich, Liq. Cryst. **24**, 117 (1998).
[3] Y. W. Inn and M. M. Denn, J. Rheol. **49**, 887 (2005).
[4] R. K. Goyal and M. M. Denn, Phys. Rev. E **75**, 021704 (2007).
[5] S. Chandrasekhar, *Hydrodynamic and Hydromagnetic Stability* (Oxford University Press, London, 1961).
[6] S. Tomotika, Proc. R. Soc. London, Ser. A **150**, 322 (1935).
[7] A. Rey, J. Phys. II **7**, 1001 (1997).
[8] M. Kleman and O. D. Lavrentovich, *Soft Matter Physics* (Springer, New York, 2003), Chap. 5.
[9] P. P. Karat and N. V. Madhusudana, Mol. Cryst. Liq. Cryst. **36**, 51 (1976).
[10] R. D. Polak, G. P. Crawford, B. C. Kostival, J. W. Doane, and S. Zumer, Phys. Rev. E **49**, R978 (1994).
[11] T. De'nève, M. Kleman, and P. Navard, Liq. Cryst. **18**, 67 (1995).
[12] G. P. Crawford and S. Žumer, Int. J. Mod. Phys. B **9**, 2469 (1995).
[13] J. Nehring and A. Saupe, J. Chem. Phys. **54**, 337 (1971).
[14] A. Rapini and M. Papoular, J. Phys. (Paris), Colloq. **30**, C4 (1969).
[15] G. P. Crawford, D. W. Allender, and J. W. Doane, Phys. Rev. A **45**, 8693 (1992).
[16] T. Gruhn and S. Hess, Z. Naturforsch., A: Phys. Sci. **51**, 1 (1996).
[17] A. M. Smondyrev and R. A. Pelcovits, Liq. Cryst. **26**, 235 (1999).
[18] E. Berggren, C. Zannoni, C. Chiccoli, P. Pasini, and F. Semeria, Phys. Rev. E **50**, 2929 (1994).
[19] G. Fuller, *Optical Rheometry of Complex Fluids* (Oxford University Press, New York, 1995).
[20] C. Chiccoli, P. Pasini, E. Berggren, and C. Zannoni, Mol. Cryst. Liq. Cryst. Sci. Technol., Sect. A **290**, 237 (1996).
[21] P. K. Rai, M. M. Denn, and C. Maldarelli, Langmuir **19**, 7370 (2003).
[22] G. Rueda and M. T. Shaw, *SPE ANTEC Conference Proceedings* (Society of Plastics Engineers, Brookfield, Connecticut, 1991), Vol. 37, p. 2005.